THE JOURNAL OF CHEMICAL PHYSICS **143**, 124201 (2015)

Direct assignment of molecular vibrations via normal mode analysis of the neutron dynamic pair distribution function technique

A. M. Fry-Petit,[1,2,3,a),b)] A. F. Rebola,[4] M. Mourigal,[2,c)] M. Valentine,[2] N. Drichko,[2]
J. P. Sheckelton,[1,2,3] C. J. Fennie,[4] and T. M. McQueen[1,2,3,a)]
[1]*Department of Chemistry, The Johns Hopkins University, Baltimore, Maryland 21218, USA*
[2]*Institute for Quantum Matter and Department of Physics and Astronomy, The Johns Hopkins University, Baltimore, Maryland 21218, USA*
[3]*Department of Materials Science and Engineering, Johns Hopkins University, Baltimore, Maryland 21218, USA*
[4]*Department of Applied Physics, Cornell University, Ithaca, New York 14853, USA*

(Received 26 May 2015; accepted 21 August 2015; published online 23 September 2015)

For over a century, vibrational spectroscopy has enhanced the study of materials. Yet, assignment of particular molecular motions to vibrational excitations has relied on indirect methods. Here, we demonstrate that applying group theoretical methods to the dynamic pair distribution function analysis of neutron scattering data provides direct access to the individual atomic displacements responsible for these excitations. Applied to the molecule-based frustrated magnet with a potential magnetic valence-bond state, $LiZn_2Mo_3O_8$, this approach allows direct assignment of the constrained rotational mode of Mo_3O_{13} clusters and internal modes of MoO_6 polyhedra. We anticipate that coupling this well known data analysis technique with dynamic pair distribution function analysis will have broad application in connecting structural dynamics to physical properties in a wide range of molecular and solid state systems. © *2015 AIP Publishing LLC.* [http://dx.doi.org/10.1063/1.4930607]

I. INTRODUCTION

Molecular vibrations, or their periodic lattice version phonons, underpin phase transitions, and many physical properties of materials including optical, electronic, and magnetic responses.[1] Consequently, to construct structure-function relationships in materials, it is essential to determine both the energy and atomic character of the vibrational modes. Infrared, Raman, and related spectroscopic techniques are routinely used to probe the energy of the vibrational transitions of molecules. Through detailed normal mode analysis and comparison to a range of related compounds, the atomic character of each transition can then be determined.[2,3] These methods are also used to probe periodic solids, providing the energy of their phonon modes and exposing the effect of the crystal lattice on the vibrational modes of their constituting moieties.[4] In particular, inelastic neutron scattering is used in solids to observe the vibrational transitions in reciprocal space, beautifully mapping the fast dispersing acoustic modes, but often not garnering as much insight into the narrow more local modes.[5] All of these techniques robustly assign the energies of different vibrations, but none provide the same direct access to the atomic motions responsible for specific excitations as achieved by using the dynamic pair distribution function (DPDF) method.

DPDF is a technique that complements other dynamic techniques by probing local dynamics in both long range and short range structures. If one is interested only in local dynamics IR, and Raman spectroscopy can be used to probe that, but these spectroscopic techniques lack the momentum resolution that is provided in an inelastic neutron experiment. However, traditional analysis of inelastic neutron experiments favors the study of highly dispersive modes while not providing much insight into the local modes. DPDF is able to probe relatively flat phonon bands by taking the Fourier transform of the total scattering and thus providing the local atomic correlations at discrete energy transfers constrained only by the resolution of the energy transfer.[6,7]

The roots of DPDF are found in the neutron dynamic pair correlation function (DPCF) method first explored by the amorphous materials' community.[8–12] DPCF was theorized to fill an experimental gap by providing insight into the dynamics of amorphous materials that, due to their lack of long range order, are hard to study with inelastic spectroscopy.[8] These early studies, including studies on crystalline cuprate superconductors,[12,13] showed the benefit of visualizing the local dynamics such as changes in coordination environment and the phase of atomic motions between atomic correlations in amorphous materials where the motions are not constrained by a long range crystal lattice. The DPDF method was first outlined by McQueeney[6,14] and further discussed by others,[7,15] as a transformation of total scattering inelastic neutron data similar to DPCF, but with the added advantage of theoretically maintaining the probability information contained in the integral of the atomic correlation peaks. In addition to not preserving probability information, DPCF shows other differences from DPDF, including, for example, displaying one peak on one side of the static Gaussian for an out of phase motion versus peaks on both sides of the static Gaussian in

---

[a] Authors to whom correspondence should be addressed. Electronic addresses: mcqueen@jhu.edu and afry@fullerton.edu

[b] Current address: Department of Chemistry and Biochemistry, California State University, Fullerton, California 92831, USA.

[c] Current address: School of Physics, Georgia Institute of Technology, Atlanta, Georgia 30332, USA.

DPDF; this is a result of the weighting factor of $1/Q^2$ in the Fourier transform of DPCF.[14] The use of this transformation has resulted in successful studies of relaxor ferroelectrics, orbitally ordered ferromagnets, and superconductors.[6,16–20] Most of these studies focus on qualitative comparison of nearest neighbor correlations using discrete energy cuts or DPDF spectra interpolated over energy and/or temperature. The use of DPDF has thus been limited by the paucity of methods to interpret the resulting data.

Here, we show that well-known group theoretic methods from chemistry can be used to extract physically intuitive information from DPDF measurements. Specifically, using DPDF, combined with normal mode analysis we observe and assign the low energy constrained rotational mode of Mo_3O_{13} clusters and the internal modes of MoO_6 octahedra in the geometrically frustrated antiferromagnet $LiZn_2Mo_3O_8$ (LZMO) and its non-magnetic analog $Zn_2Mo_3O_8$ (ZMO). By doing so, we are able to test theoretical predictions[21] and put strong constraints on the origin of the puzzling "kink" observed in the magnetic susceptibility of LZMO at 96 K.[22] LZMO has recently garnered much attention due to its realization of frustrated magnetism originating from molecular clusters.[21–24] The structure of LZMO is made up of layers of $S = 1/2$ bearing Mo_3O_{13} molecular units arranged on triangular lattice planes perpendicular to the *c*-axis separated by layers of Li and Zn (Figure 3(a)). The magnetic susceptibility as a function of temperature for LZMO possesses two separate Curie-Weiss regions, which is proposed to be due to a valence-bond state. The onset of the lower temperature regime is associated with a decrease in the Curie constant to one third of its high-temperature value.[22] These interesting results have spurred several additional studies of this material[21,23–26] including the present study of the phonon induced atomic motions in real space.

II. EXPERIMENTAL

A. Materials

The sample consisted of 18.5 g of ^{7}Li enriched ^{7}LZMO powder prepared using the method described elsewhere.[22,23] The sample was pressed and sintered into 10 pellets of diameter 1.4 cm (0.55 in.) and height 0.6 cm (0.24 in.). Laboratory X-ray diffraction on the sintered pellets revealed no preferred orientation of the grains compared to the free standing powder. The sintered pellets were vertically stacked in a thin aluminum can of diameter 1.6 cm (0.625 in.). Sheets of neutron-absorbing cadmium were inserted between every two pellets to reduce multiple scattering. The sample can was sealed under an atmosphere of ^{4}He at room temperature and mounted at the bottom of a close-cycle cryostat reaching a base temperature of $T = 5$ K.

B. Inelastic neutron scattering

The inelastic neutron scattering experiment was carried out on the direct-geometry time-of-flight spectrometer Wide Angular-Range Chopper Spectrometer (ARCS) at the Spallation Neutron Source (SNS), Oak Ridge National Laboratory (ORNL).[27] The spectrometer was operated with incoming neutron energy $E_i = 160$ meV and the Fermi chopper frequency set to 600 Hz, providing an elastic energy-resolution of 6.0(1) meV (full-width at half maximum). Background contributions from the cryostat and sample can were removed by measuring an empty aluminum can in the exact same conditions as the sample. The scattering intensity as a function of momentum $Q = \hbar|Q|$ and energy-transfer $E = \hbar\omega$, $I(Q,E) = k_i/k_f\, d^2\sigma/dE_f d\Omega$ was normalized to absolute units of mb sr^{-1} meV^{-1} f.u.$^{-1}$ using the intensity of the nuclear elastic scattering at $T = 5$ K. The momentum and energy dependence of the measured scattering intensity is shown in Figure 2 for $T = 5$ K and $T = 150$ K. From this data both the DPDF and the vibrational density of states (VDOS) were calculated.

C. DFT calculations

Density functional calculations were performed using the projector augmented plane-wave method as implemented in VASP[28,29] with the Perdew-Burke-Ernzerhof (PBE) form of the exchange-correlation functional.[30] For structural relaxations and calculation of phonons, we used a $4 \times 4 \times 4$ Gamma centered **k**-point mesh and a kinetic energy cutoff of 530 eV. All forces were converged to be lower than 0.001 eV/Å.

D. Raman spectroscopy

Micro-Raman spectra of LZMO and ZMO with a resolution of 2 cm^{-1} (0.25 meV) were measured using a Jobin-Yvon T64000 triple monochromator Raman spectrometer equipped with an Olympus microscope. The 514.5 nm line of a Spectra-Physics Ar^+–Kr^+ laser was used for excitation light and the laser probe diameter at the sample was approximately ~2 μm.

III. RESULTS AND DISCUSSION

DPDF results from the Fourier transform of the appropriately normalized $S(Q,\hbar\omega)$,

$$G(r,\hbar\omega) = (2/\pi)\int_0^\infty Q\left[S(Q,\hbar\omega) - B(Q,\hbar\omega)\right] \times \sin(Qr)\, dQ, \tag{1}$$

where $S(Q,\hbar\omega)$ is the total scattering intensity as a function of energy, $\hbar\omega$, and momentum transfer, Q, and $B(Q,\hbar\omega)$ accounts for Q dependent background terms that are removed during data processing.[14] DPDF is identical in form to the well-established pair distribution function (PDF) a real-space, scattering-length weighted atom-atom histogram, but with energy resolution. Further details on the novel treatment of Q dependent background terms will appear in subsequent publications.

To present an intuitive way to visualize the effect of normal modes on DPDF as a function of energy, we simulated three different vibrational modes of a D_2 dimer centered in the LZMO unit cell. These simulations are based on the equations laid out in the work by McQueeney.[14] For the sake of this calculation, the D_2 dimer is placed at the center of the

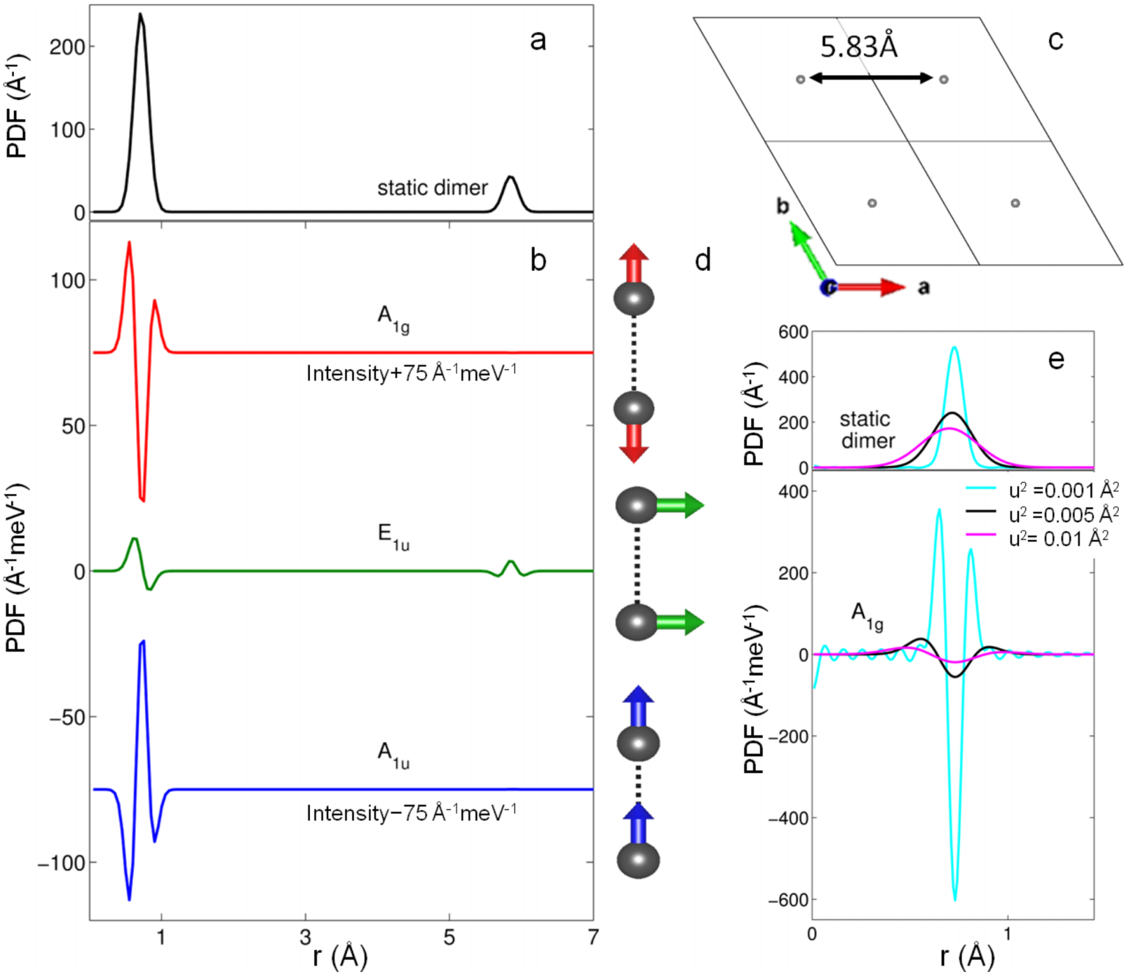

FIG. 1. The pair distribution function for a static D_2 dimer and a mean squared displacement, u^2, of 0.005 Å^2 is shown in (a) with a bond length of 0.7415 Å which is the nearest neighbor distance and is depicted as a dashed line in (d). The next nearest neighbor is at a distance of 5.83 Å as shown by the second peak in (a) and denoted by the arrow in (c) (distance derived from a dimer placed in the center of the LZMO unit cell). (b) depicts the effect of three modes on the pair distribution (offset for clarity) and (d) depicts the motion of the atoms: (1) the A_{1u} mode which is parallel to the nearest neighbor atomic correlation (blue), (2) the E_{1u} mode which is perpendicular to the nearest neighbor atomic correlation (green), and (3) the A_{1g} mode which is parallel to the nearest neighbor correlation (red). The color of the displacement vector corresponds with the lines and thus the legend. Vector lengths are not to scale. (e) demonstrates the effect of the mean squared displacement on the Gaussian static line in the top panel and the splitting of the out of phase A_{1g} motion in the bottom panel. The black lines are the same static and A_{1g} modes plotted in (a), respectively, in (e) they are overlaid with a decreased $u^2 = 0.001$ Å^2 in cyan, and an increased $u^2 = 0.01$ Å^2 in magenta.

LZMO unit cell, providing sufficient space between the nearest neighbor and next nearest neighbor to clearly show the effects of different types of atomic distortion. In this calculation the fundamental frequency of the D_2 vibration, which acts as a scalar of the PDF intensity, was set to 386.33 meV[31] for all three vibrations. This allows for the separation of the effects of intensity scaling from energy and those effects that arise from displacements. This calculation also does not account for the displacement lifetime but treats the displacement as a delta function. Figure 1(a) depicts simulations of the PDF for the static D_2 dimer, $G(r,\hbar\omega = 0)$, and Figure 1(b) depicts the simulations of the three D_2 dimer normal modes, $G(r,\hbar\omega \neq 0)$, offset by a constant value for clarity.

The simulation of the static PDF shows two peaks centered at the nearest neighbor distance, 0.7415 Å, and the next nearest neighbor distance, 5.83 Å. The area under curve is related to the number of atom-atom pairs separated by that distance normalized by shell surface area. Figure 1(d) shows schematics of the applied atomic displacements in the $D_{\infty h}$ point group of the D_2 molecule, A_{1g} (optic mode), E_{1u} (perpendicular acoustic mode), and the A_{1u} (parallel acoustic mode), and their effect on the PDF in Figure 1(b). When the displacement vector lies along a given atom-atom correlation, it has the largest effect on the PDF intensity for that correlation but falls off as $1/r^2$. Focusing on the nearest neighbor distance, in-phase motions like the A_{1u} mode and the out-of-phase A_{1g} mode result in a removal of some intensity to the left and right of the static peak (narrowing) and a splitting of the static peak (broadening), respectively. Narrowing is observed at the next nearest neighbor distance for the E_{1u} mode, because this motion while perpendicular to the nearest neighbor atom-atom correlation is parallel to the next nearest neighbor atom-atom correlation. Conversely, any motion that is perpendicular to the atom-atom correlation results in a small shift of the peak. Thus, very little contribution to the nearest neighbor atom-atom correlation comes from the E_{1u} mode and very weak (unobservable on this scale) contribution to the next nearest neighbor atom-atom correlation in A_{1g} and A_{1u} modes. To ensure that the magnitude of displacement does not affect the peak shape or location several simulations were done where

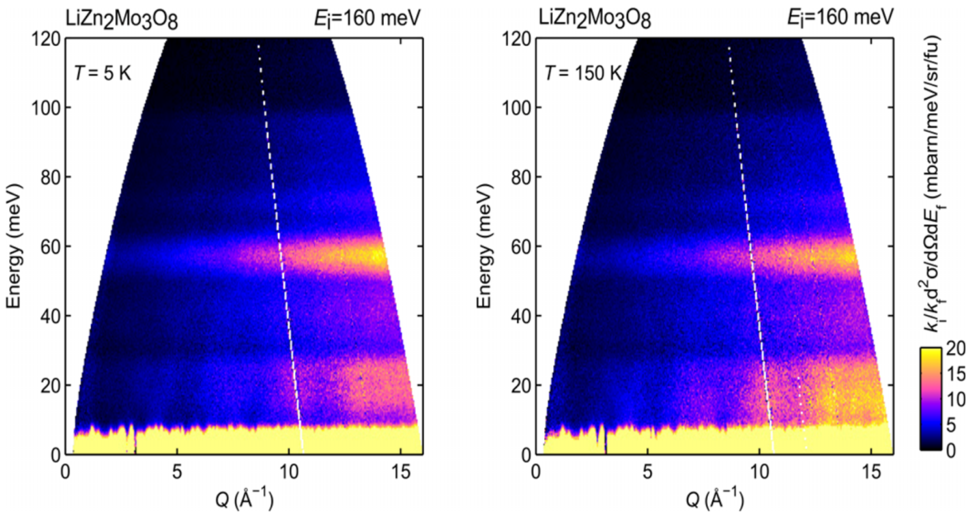

FIG. 2. Powder inelastic scattering from LZMO at T = 5 K (left) and T = 150 K (right) collected with an E_i = 160 meV. Cadmium baffles that are installed in ARCS to decrease detector cross talk results in zero intensity reaching some of the detector banks; this appears as white lines in this figure. These banks are removed via a nearest neighbor interpolation before the transformation to the DPDF.

atoms were sequentially moved further apart in the A_{1g} mode. However, no change was seen in the DPDF confirming that magnitude is only encapsulated in the phonon lifetime term and will just scale the intensity and spread over energy. Since all of the modes result in radically different DPDFs, regardless of the magnitude of the displacement, in principle the normal modes from symmetry analysis can be mapped onto the atom-atom correlations. To experimentally show the utility of this technique, we probed the local vibrational modes of a system hypothesized to form an interesting magnetic valence bond state, LZMO.

Raw total inelastic neutron scattering for LZMO at 5 K and 150 K is shown in Figure 2 and no significant difference is seen between the phonon spectra beyond the difference in thermal population. The flat bands present at approximately 10-30 meV, 30-50 meV, and 50-60 meV are indicative of local motion. To get real space insight into the local dynamics of the materials, the Fourier transform at discrete energies is taken to generate the DPDF. The energy discriminant nature of the measurement allows the isolation of a purely elastic (no energy transfer) PDF. We refer to this quantity, $G(r,\hbar\omega = 0)$, as the static PDF but it has been previously referred to as the average PDF, as it shows the time average of the probability of two atoms being some distance apart.[6,7] The nomenclature has been changed to static PDF to capture that $G(\mathrm{r},\hbar\omega = 0)$ is a PDF that excludes changes in the atomic-correlations due to phonons within the energy resolution of the measurement and thus only capturing any zero point motion. In a PDF where all excited phonon modes are included is now referred to as the total integrated PDF (previously instantaneous PDF[6,7]) to clearly portray that it is generated by integrating over all available energy transfers. This is the form of a typical PDF where energy discrimination is not possible. The qualitative analysis of the static PDF and total integrated PDF data provides increased understanding into LZMO. As discussed by others,[6,7] the difference in peak shapes between the static and the totally integrated PDFs (Figure 3(b)) demonstrates that phonons, captured in the totally integrated PDF, significantly contribute to $G(r)$ and would typically be included in a conventional PDF analysis.[6] To accurately probe for local structural changes free of phonon induced atomic displacements in the two different Curie-Weiss regimes of LZMO, least squares refinement to the static PDF data, $G(r,\hbar\omega = 0)$, at $T = 150$ K in the R-3m model using PDFgui[32] was performed, Figure 3(c). The refinement removed all of the R-3m symmetry elements, thereby dropping the structure down to $P1$. This allowed for unconstrained movements of the atoms. However, upon inspection of the atomic parameters with VESTA[33] there is no lowering of symmetry from R-3m within a tolerance of 1×10^{-4} Å. The refined R-3m structural parameters are listed in Table S1,[38] which are in good agreement with recent PDF studies.[26] Additionally, no significant difference in the static local structure was observed between $T = 150$ K and $T = 5$ K (Figure 3(d)).

Additional detailed local information that captures the atomic dynamics can be gleaned from the inelastic portion of the spectrum. The DPDF for LZMO at $T = 150$ K is shown in Figure 4 and is compared to the both the Raman spectra and VDOS. It is important to note that the intensity of the response can appear inequivalent between neutron spectroscopy, both DPDF and VDOS, and Raman spectroscopy due to the difference in the scattering mechanism between Raman and neutrons; the intensity of the Raman mode is due to the photon induced polarizability of the mode while the atomic motion observed via DPDF is weighted by the atomic neutron scattering-length.

Remarkably, changes in the DPDF at finite energy transfer coincide with excitations observed by Raman spectroscopy, Figure 4. Assignment of the vibrational mode corresponding to each excitation proceeds in several steps. First, standard chemical point group methods are used to generate all possible symmetry-adapted vibrational modes. Then, for each of these modes, the expected changes in the atom-atom distribution function are predicted by determining which atom-atom correlations (which are atom-pair correlations that are calculated based on the long range crystal structure and are shown in Figure S2[38]) lie along the displacement vector and if those motions would be in- or out-of-phase with one another. Raman data for this system show good agreement with the changes in the DPDF thus allowing the assignments to be constrained by selection rules that would

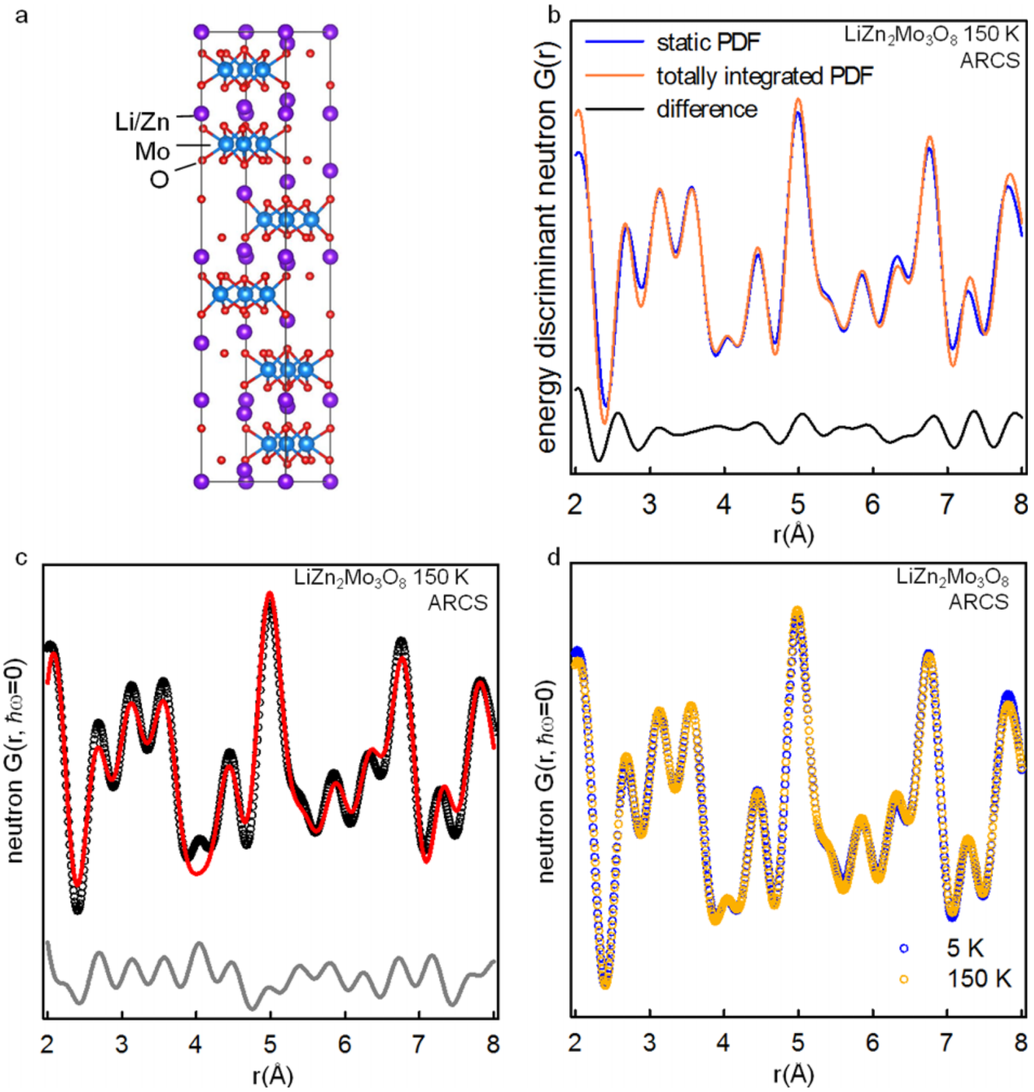

FIG. 3. (a) Structure of LZMO viewed perpendicular to c-axis to highlight the Mo_3O_8 (blue and red) layers that are separated by disordered Li and Zn ions (purple). (b) Totally integrated PDF (yellow), $E_{range} = -160$ to 160 meV, versus static PDF (blue) scaled by the ratio of the mean totally integrated G(r) to the mean of the static G(r) for LZMO 150 K data collected on ARCS with an $E_i = 160$ meV. Scaled static PDF is the static PDF multiplied by the ratio of the average of the totally integrated PDF intensity to the average of the static PDF intensity. (c) Least squares refinement (red line) of the long range structure to the 150 K static neutron $G(r)$ (black circles) of LZMO with the difference curve shown in gray from data collected on ARCS with an $E_i = 160$ meV. (d) LZMO static PDF data of 5 K (yellow circles) and 150 K (blue circles) collected on ARCS overlaid to show no deviation in local crystallographic structure above and below the "kink" in the susceptibility data. Negligible thermal sharpening is observed between the two different temperatures, indicative of similar Debye-Waller factor between the temperatures which could be present because while the static line is narrow, it is not finite and thus may include thermal motion.

not typically constrain neutron spectroscopy. Finally, these can be compared to constant-energy DPDF slice to make an assignment (Figure 6). For example, the mode at ∼47 meV in LZMO clearly shows a splitting of the O–O atom-atom correlations (marked by g in Figure 6 and Figure S3 with atom-atom correlations shown in Figure S2[38]) within the Mo_3O_{13} clusters which is only consistent with the oxygen A_{1g} mode of the D_{3d} point group, shown in Figure 5(IVa) or 5(IVb). This mode possesses displacement vectors that have some component in three directions relative to O–O atom-atom correlation; however as shown in Figure 5(IVb), a portion of the displacement vector lies along the O–O atom-atom correlation. This is similar to the extreme A_{1g} mode depicted in Figure 1 where the entire out of phase motion lies along the atom-atom correlation and thus in this case causes the splitting of the O–O atom-atom correlation most clearly observed in the stacked energy cuts, Figures 6 and S3.[38] The splitting in atom-atom correlations can at first glance seem to be too large of atomic motion to be physical; however, the splitting is a result of intensity being given to the edges of the static peak and removed from the center of the peak.[14] The magnitude of splitting is given by the breadth of the static peak, which is defined by both the Q range of the measurement and the mean squared displacement, u^2.[14] This is demonstrated in Figure 1(e) by altering the mean squared displacement from $u^2 = 0.005$ Å^2 in Figure 1(a) to $u^2 = 0.001$ Å^2 (cyan) and $u^2 = 0.01$ Å^2 (magenta) in Figure 1(e). When the mean squared displacement is decreased (or Q range increased) the static Gaussian is narrower, and thus the split peaks in the A_{1g} mode are also closer together. The converse is true with the mean squared displacement is increased (or Q range decreased). The ∼47 meV internal mode of the octahedra

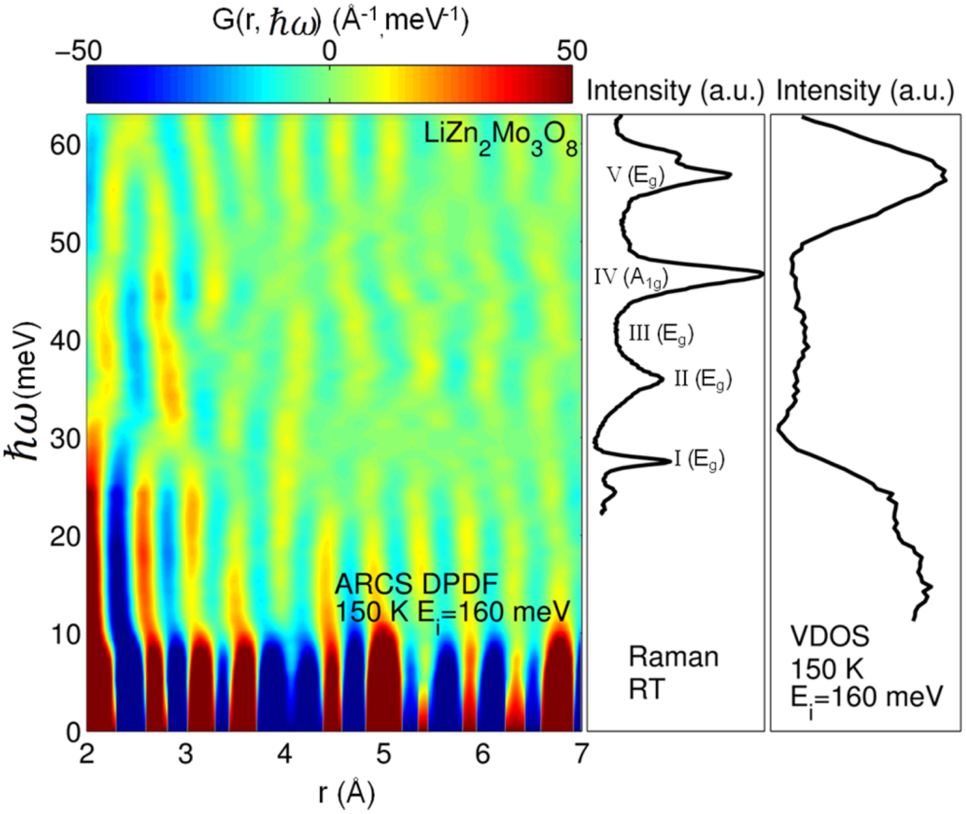

FIG. 4. Energy-resolved pair distribution function of LZMO (150 K) (left) is compared with spectroscopic Raman data (room temperature) (center), and the VDOS 150 K (Q_{range} = 2-13.9 Å) (right) for the same compound. Roman numerals and spectroscopic assignments are addressed in more detail in Figure 5 and Table I.

(Figure 5(IV)) is consistent, both in energy and in shape of the band, with the υ_5 oxygen bending mode observed in perovskite *B* site octahedra.[4] Using this group theoretical approach (Figure 5), additional internal modes of the MoO_6 octahedra were assigned to the energy range from 50 meV to 60 meV (Figure 5(V)). The 25 meV mode shows a dynamic rotation of the clusters, Figure 5(I), that is marked by the narrowing of the two separate O–O atom-atom correlations into a single correlation length. The other modes observed in the 27 meV–35 meV energy range (Figures 5(IIa) and 5(IIb)) and the 35 meV–45 meV energy range (Figures 5(IIIa) and 5(IIIb)) are assigned to multiple internal cluster E_g vibrations. These assignments are a remarkable demonstration that LZMO is a molecular solid built of Mo_3O_{13} molecular units.

To confirm these assignments, we used first principles electronic structure calculations. The calculations were done on ZMO (DPDF in Figure S1 of the supplementary material[38]) in the LZMO structure due to the difficulties in treating open shell insulating materials. Once the atomic displacement of each mode was determined, the same calculation that was done on the D_2 dimer (Figure 1) was performed to generate the calculated DPDF for each energy cut. For the simulation of the DPDF for ZMO, the appropriate energy was used to scale the data according to the work by McQueeney[14] and no approximation of the phonon lifetime was used. Good

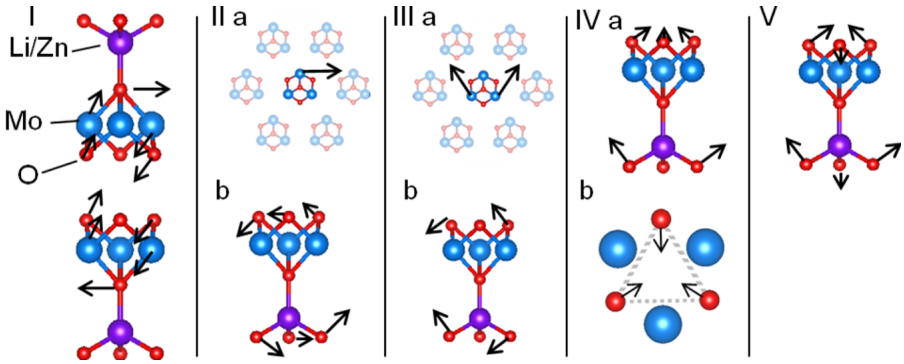

FIG. 5. All of the labels cross reference with Table I. (I) depicts an E_g mode that causes splitting of O–O and Zn–O bond lengths, (II) depicts an E_g mode of a Mo_3O_{13} cluster, (IIa), motion of Mo resulting in a convergence of the inter- and intra-cluster Mo–Mo bond lengths and out of plane motions of oxygen, (IIb), resulting in a splitting of Mo–O bond lengths. (III) also depicts an E_g mode separated into in plane, (IIIa) Mo motions resulting in a Mo–Mo bond length condensation and an out of plane, (IIIb) oxygen vibration that splits the Mo–O bond lengths and the third coordination sphere of the O–O correlations. (IVa) or (IVb) and (V) both depict oxygen bending modes that result predominantly in a change in the O–O bond lengths but also show a Mo–O and (Zn/Li)–O mode and the next-next-nearest neighbor Zn/Li in (V). (IVb) depicts the Mo and O in the layer above when the cluster is viewed from the top down; the dashed lines are used to highlight the O–O nearest neighbor distances that are discussed in depth in the description of the mode assignments.

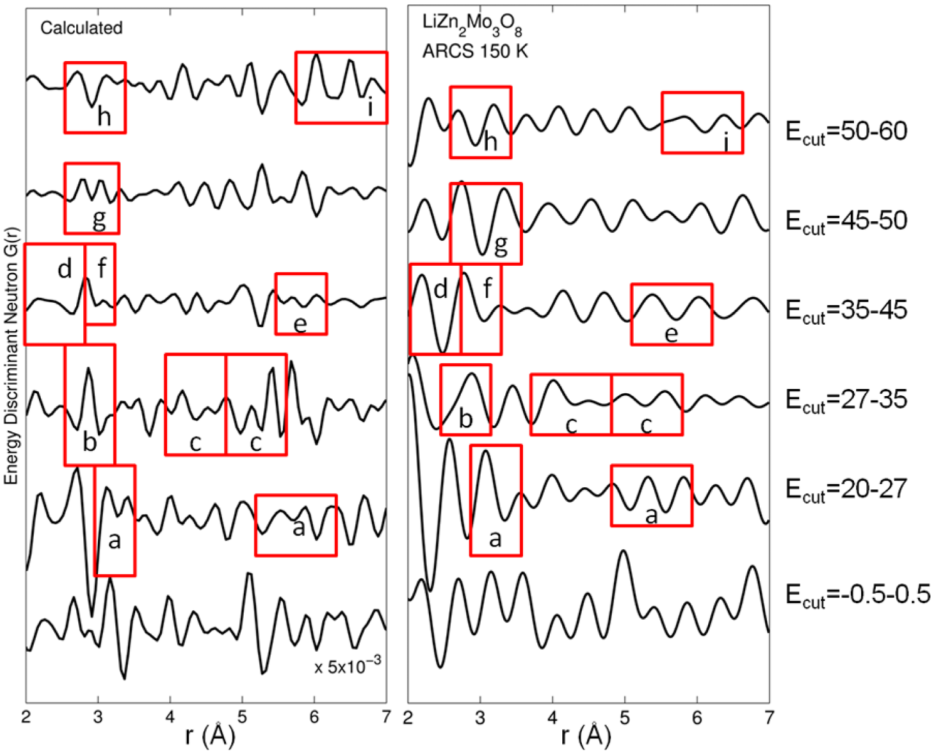

FIG. 6. Calculated (left) and experimental (right) energy discriminant neutron $G(r)$. Atomic correlations are marked with boxes corresponding to the descriptions listed in Table I.

qualitative agreement (Table I and Figure 6) between observed and predicted mode energies for these specific modes supports our group theoretical DPDF analysis method. Splitting or broadening of peaks is marked in the calculation and the experimental by boxes (a), (c), (d), (e), (g), (h), and (i), and convergence of the Mo–Mo in the xy plane is marked in the calculation with (b) and (f).

Comparison of VDOS and DPDF shows that there is a broad band in the VDOS ranging from 10 to 30 meV where very little change is seen in the DPDF except where there is a coincident Raman band. What is clearly observed is that above the elastic bleed that reaches to just below 10 meV, there is a shift in the atom-atom correlations to lower r. This is expected and is a manifestation of the fast-dispersing long-range acoustic modes that are perpendicular to the most local atomic correlations, just as depicted as the E_{1u} mode of D_2 (Figure 1). The elastic bleed results in the inelastic spectrum below ~10 meV being dominated by the elastic PDF spectra, obscuring the true inelastic signals in that energy range and is a consequence of the relatively large incident energies used to reach higher Q values. The elastic bleed limits the resolution of DPDF at lower energy transfers.

One of the limitations to DPDF is that increasing the incident energies to access a Q-range that is more conducive to PDF analysis than typical inelastic neutron experiments is a decrease in energy resolution and an increase in elastic bleed. In LZMO the interesting kink in the magnetic susceptibility data occurs around 90 K (~7.8 meV); however, this energy range is not accessible with the higher E_i = 160 meV. To probe if there was additional changes in the DPDF below 10 meV that may correspond to the magnetic transition,[22] the DPDF with an E_i = 80 meV was calculated and compared to the DPDF with an E_i = 160 meV, both truncated at the same Q for appropriate comparison (Figure 7). Visual comparison of the two DPDF reveals no additional changes, and thus, no additional dynamic information is gleaned from the lower E_i

TABLE I. Values of the DFT calculated and observed Raman bands for ZMO and LZMO with the description of the atomic motions associated with that mode. The atomic motions are labeled with letters that correspond to the boxes marking the atomic motions in Figures 6 and S3.[38]

Region and mode	Calculated (meV)	$Zn_2Mo_3O_8$ (meV)	$LiZn_2Mo_3O_8$ (meV)	Description of atomic motions
I(E_g)	27.0	26.3	24.6	(a) O–O bond length split between layers and within the tetrahedra
II(E_g)	33.4	33.6	27.7	(b) Convergence of Mo–Mo in xy plane (c) Splitting of Mo–O perpendicular to the z-axis
III(E_g)	35.8	40.4	36.0	(d) Splitting of Mo–O bond lengths (e) Splitting of the 3rd coordination sphere O–O perpendicular to z-axis
	42.4	42.5	40.8	(f) Convergence of Mo–Mo in xy plane
IV(A_{1g})	44.6	46.0	46.9	(g) Splitting of O–O bond lengths
V(E_g)	54.9	54.9	56.9	(h) Splitting of O–O bond lengths
	58.2	58.9	58.8	(i) 2nd coordination sphere Zn–O smearing of bond lengths

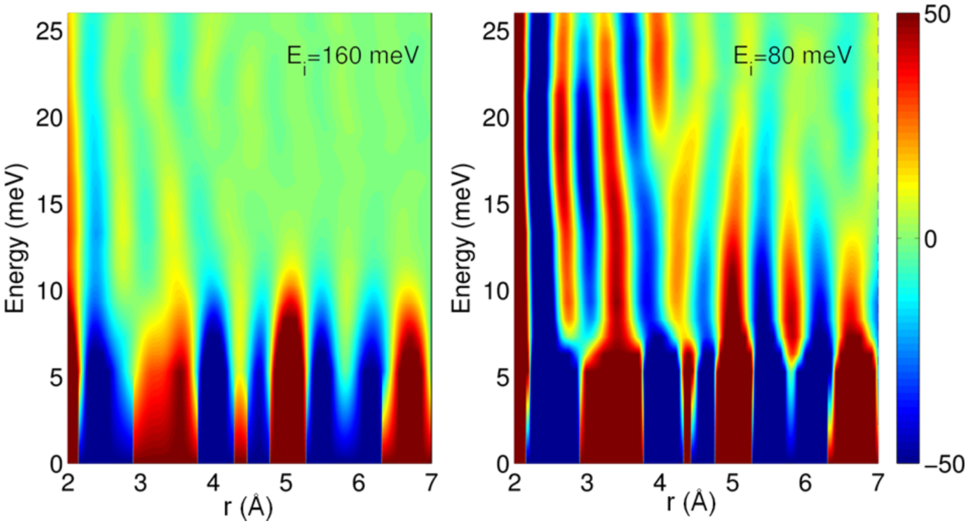

FIG. 7. 150 K DPDF for $E_i = 160$ meV (left) and $E_i = 80$ meV (right) to ensure that the DPDF does not change at lower as the energy resolution is improved at energies closer to the transition temperature.

DPDF. The differences in intensity is a result of the energy range of phonons being double for the $E_i = 160$ meV and thus the intensity being lower than that of the DPDF with an $E_i = 80$ meV.

In addition to demonstrating the utility of normal mode analysis through the assignment of the series of vibrational modes from 25 meV to 60 meV, the analysis of the static PDFs provides important insight into the physics of LZMO. Previous theoretical work has suggested that the formation of a valence-bond singlet (and candidate spin-liquid) state in LZMO originates from rotations of the Mo_3O_{13} cluster units.[21] The static PDF (Figure 3(c)) rules out static rotations or other local structural distortions expected if a static valence-bond state was formed. Further, the energy of the lowest rotational mode, mode I at 27 meV, is too high to account for effects on the primary magnetic exchange energy scale of 18 meV.[22,24] Additionally, both non-magnetic ZMO and magnetic LZMO show the same local atomic motions at very similar energies (Figures S1[38] and 4); this rules out magnetically driven lattice dynamics such as a Peierls distortion or a spin Jahn-Teller effect. As previous work has found single ion physics is unlikely to be responsible for the magnetic behavior of LZMO,[23] we are left to conclude that the "kink" in the susceptibility of LZMO reflects an intrinsic crossover of purely electronic or magnetic origin.

A comparison of DPDF with normal mode analysis to complimentary approaches is warranted. Uniquely, the DPDF method gives direct access to the atomic pairwise correlations responsible for a given excitation. This information cannot be gleaned from the totally integrated data (Figure 3(b)) as the vibrational contribution from multiple phonon modes can combine destructively when energy integrated. Other methods can probe different aspects of the structural dynamics, such as using multi-dimensional IR to probe the coupling of quantum states,[34] use of an electron microscope for spatially resolved vibrational spectroscopy,[35] and time-resolved diffraction used to probe changes in the long range average structure in response to external stimuli.[36,37] However, none of the aforementioned methods provide direct unfettered access to the atomic motions in real space like DPDF does. Our contribution here is to show that interpretation of the DPDF need not be purely qualitative[16] nor require significant simulation and computation. The use of symmetry-adapted mode analysis we have demonstrated here is straightforward, based on well-known chemical principles, and allows connection to the previous century of understanding molecular motions.

IV. CONCLUDING REMARKS

In short, using symmetry adapted mode analysis, we are able to directly interpret the DPDF data of LZMO and ZMO and unequivocally assign particular vibrational modes to specific excitations. In the case of LZMO, DPDF allows us to rule out static or dynamic rotational modes of the Mo_3O_{13} molecular units as the origin of the formation of the valence-bond state[21] and to show how lattice dynamics, independent of spin Jahn-Teller or Peierls type effects, can conspire to produce unconventional magnetic ground states. More generally, it demonstrates the robustness of DPDF as a probe to be applied beyond condensed matter physics and into molecular systems when combined with normal mode analysis. We expect future improvements in neutron instrumentation will further increase the ability of this technique to assess the local atomic correlations responsible for individual vibrations. Vibrational transitions are present in any material above absolute zero, and those vibrations are the source of many important properties; therefore, the ability to visualize the dynamics of atomic correlations through DPDF using symmetry-adapted mode analysis will provide new insight into these vastly important vibrational processes.

ACKNOWLEDGMENTS

The authors want to thank O. Tchernyshyov for helpful discussions and the ARCS beam line scientist, Doug Abernathy, for his assistance with the experiment. This work was funded by the David and Lucile Packard Foundation and the Institute for Quantum Matter, supported by the U.S. Department of Energy, office of Basic Energy Sciences, Division of Material Sciences and Engineering under Grant No. DE-FG02-08ER46544. Use of the Spallation Neutron Source (SNS) is supported by the Division of Scientific User Facilities, Office of Basic Energy Sciences, U.S. Department of Energy, under Contract No. DE-AC05-00OR22725 with UT-Battelle, LLC.

[1] J. Gersten and F. Smith, *The Physics and Chemistry of Materials* (John Wiley & Sons, Inc., New York, NY, USA, 2001).

[2] F. Cotton and G. Wilkinson, *Advanced Inorganic Chemistry: A Comprehensive Text*, 3rd ed. (John Wiley & Sons, Inc, 1972).

[3] K. Nakamoto, *Infrared and Raman Spectra of Inorganic and Coordination Compounds*, 6th ed. (John Wiley & Sons, Inc, 2009).

[4] M. Liegeois-Duyckaerts and P. Tarte, Spectrochim. Acta, Part A **30**, 1771 (1974).

[5] G. Shirane, S. M. Shapiro, and J. M. Tranquada, *Neutron Scattering with a Triple-Axis Spectrometer* (Cambridge University Press, 2004).

[6] R. McQueeney, "Lattice effects in high-temperature superconductors," Ph.D. dissertation (University of Pennsylvania, 1996).

[7] T. Egami and S. J. L. Billinge, *Underneath the Bragg Peaks: Crystallographic Analysis of Complex Materials* (Elsevier, 2012).

[8] J. M. Carpenter and C. A. Pelizzari, Phys. Rev. B **12**, 2397 (1975).

[9] A. C. Hannon, M. Arai, R. N. Sinclair, and A. C. Wright, J. Non-Cryst. Solids **150**, 239 (1992).

[10] M. Arai, A. C. Hannon, A. D. Taylor, A. C. Wright, R. N. Sinclair, and D. L. Price, Phys. B **181**, 779 (1992).

[11] A. C. Hannon, M. Arai, and R. G. Delaplane, Nucl. Instrum. Methods Phys. Res., Sect. A **354**, 96 (1995).

[12] M. Arai, K. Yamada, S. Hosoya, A. C. Hannon, Y. Hidaka, A. D. Taylor, and Y. Endoh, J. Supercond. **7**, 415 (1994).

[13] M. Arai, A. C. Hannon, T. Otomo, A. Hiramatsu, and T. Nishijima, J. Non-Cryst. Solids **192-193**, 230 (1995).

[14] R. McQueeney, Phys. Rev. B **57**, 10560 (1998).

[15] T. Egami and W. Dmowski, Z. Kristallogr. **227**, 233 (2012).

[16] W. Dmowski, S. Vakhrushev, I.-K. Jeong, M. Hehlen, F. Trouw, and T. Egami, Phys. Rev. Lett. **100**, 137602 (2008).

[17] H. Takenaka, I. Grinberg, and A. Rappe, Phys. Rev. Lett. **110**, 147602 (2013).

[18] B. Li, D. Louca, B. Hu, J. L. Niedziela, J. Zhou, and J. B. Goodenough, J. Phys. Soc. Jpn. **83**, 084601 (2014).

[19] D. Louca, K. Horigane, A. Llobet, R. Arita, S. Ji, N. Katayama, S. Konbu, K. Nakamura, T.-Y. Koo, P. Tong, and K. Yamada, Phys. Rev. B **81**, 134524 (2010).

[20] K. Park, J. W. Taylor, and D. Louca, J. Supercond. Novel Magn. **27**, 1927 (2014).

[21] R. Flint and P. A. Lee, Phys. Rev. Lett. **111**, 217201 (2013).

[22] J. P. Sheckelton, J. R. Neilson, D. G. Soltan, and T. M. McQueen, Nat. Mater. **11**, 493 (2012).

[23] M. Mourigal, W. T. Fuhrman, J. P. Sheckelton, A. Wartelle, J. A. Rodriguez-Rivera, D. L. Abernathy, T. M. McQueen, and C. L. Broholm, Phys. Rev. Lett. **112**, 027202 (2014).

[24] J. P. Sheckelton, F. R. Foronda, L. Pan, C. Moir, R. D. McDonald, T. Lancaster, P. J. Baker, N. P. Armitage, T. Imai, S. J. Blundell, and T. M. McQueen, Phys. Rev. B **89**, 064407 (2014).

[25] G. Chen, H. Kee, Y. B. Kim, and I. Lizn, e-print arXiv:1408.1963v2 (2014).

[26] J. P. Sheckelton, J. R. Neilson, and T. M. McQueen, Mater. Horiz. **2**, 76 (2015).

[27] D. L. Abernathy, M. B. Stone, M. J. Loguillo, M. S. Lucas, O. Delaire, X. Tang, J. Y. Y. Lin, and B. Fultz, Rev. Sci. Instrum. **83**, 015114 (2012).

[28] G. Kresse, Phys. Rev. B **54**, 11169 (1996).

[29] G. Kresse and J. Hafner, Phys. Rev. B **47**, 558 (1993).

[30] J. P. Perdew, K. Burke, and M. Ernzerhof, Phys. Rev. Lett. **77**, 3865 (1996).

[31] K. P. Huber and G. Herzberg, *Molecular Spectra and Molecular Structure. IV. Constants of Diatomic Molecules* (Van Nostrand Reinhold Company, 1979).

[32] C. L. Farrow, P. Juhas, J. W. Liu, D. Bryndin, E. S. Božin, J. Bloch, T. Proffen, and S. J. L. Billinge, J. Phys.: Condens. Matter **19**, 335219 (2007).

[33] K. Momma and F. Izumi, J. Appl. Crystallogr. **44**, 1272 (2011).

[34] A. Stolow and D. M. Jonas, Science **305**, 1575 (2004).

[35] O. L. Krivanek, T. C. Lovejoy, N. Dellby, T. Aoki, R. W. Carpenter, P. Rez, E. Soignard, J. Zhu, P. E. Batson, M. J. Lagos, R. F. Egerton, and P. A. Crozier, Nature **514**, 209 (2014).

[36] K. Moffat, Faraday Discuss. **122**, 65 (2003).

[37] R. Mankowsky, A. Subedi, M. Först, S. O. Mariager, M. Chollet, H. T. Lemke, J. S. Robinson, J. M. Glownia, M. P. Minitti, A. Frano, M. Fechner, N. A. Spaldin, T. Loew, B. Keimer, A. Georges, and A. Cavalleri, Nature **516**, 71 (2014).

[38] See supplementary material at http://dx.doi.org/10.1063/1.4930607 for full and energy cut DPDF of $Zn_2Mo_3O_8$ and the calculated atomic pair correlations for $LiZn_2Mo_3O_8$.